Research article

Journal of RAMAN SPECTROSCOPY

Received: 1 August 2012 Revised: 1 October 2012 Accepted: 7 October 2012 Published online in Wiley Online Library: 18 March 2013

(wileyonlinelibrary.com) DOI 10.1002/jrs.4210

Two-dimensional stimulated ultraviolet resonance Raman spectra of tyrosine and tryptophan: a simulation study

Hao Ren, Jason D. Biggs and Shaul Mukamel*

We report an *ab initio* simulation study of the ultrafast broad bandwidth ultraviolet stimulated resonance Raman spectra (SRRS) of L-tyrosine, L-tryptophan, and *trans*-L-tryptophan-L-tyrosine (WY) dipeptide. Two-pulse one-dimensional SRRS and three-pulse two-dimensional SRRS that reveal inter-residue and intra-residue vibrational correlations are simulated using electronically resonant or pre-resonant pulse configurations that select the Raman signal and discriminate against excited state pathways. Multimode effects are incorporated via the cumulant expansion. The two-dimensional SRRS technique is more sensitive to residue couplings than spontaneous Raman. Copyright © 2013 John Wiley & Sons, Ltd.

Supporting information may be found in the online version of this article.

Keywords: two-dimensional; UV stimulated resonance Raman; aromatic; tyrosine; tryptophan

Introduction

Raman spectroscopy can provide detailed information on the structure and dynamics of molecules and molecular complexes, thanks to the sensitivity of vibrations to the local chemical environment.[1,2] Resonance Raman spectroscopy selectively enhances those vibrational modes that are strongly coupled to the selected electronic transition. Ultraviolet resonance Raman (UVRR) has been a powerful tool in the study of protein secondary structure.[3–11] Unlike infrared spectra, peptide resonance Raman bands of proteins do not overlap with vibrational modes of water, making them suitable for biological systems in aqueous environment. Deep UV (≤210 nm) photons excite the π–π^* transitions of the protein backbone and show strong activity of the AmI, AmII, AmIII, and C_α–H modes, which depend on the secondary structure. Asher *et al.* had developed empirical relationships between the AmIII frequencies and the Ramachandran Ψ angles of proteins. The secondary structure of complex proteins can be obtained by deconvoluting the AmIII peaks.[7,8,10] With the help of hydrogen–deuterium exchange, hydrogen-bonded N–H atoms can be distinguished in a protein.[7,11–13] Lednev *et al.* used deep UVRR technique to distinguish the fibril core structure of parallel and antiparallel amyloid fibrils.[7,11] The present study focuses on the near UV (280∼210 nm) π–π^* transitions of aromatic side chain residues, which are well separated from the deep UV peptide n–π^* and π–π^* excitations. Spontaneous Raman signals from tryptophan and tyrosine residues are often used as structural markers of proteins.[14–16]

Ultrafast broadband coherent Raman spectroscopy is widely employed to investigate the dynamics of intramolecular and intermolecular vibrational modes.[17–23] One-dimensional stimulated resonance Raman (1DSRR) signals are obtained by varying the time delay t_1 between two ultrafast pump and probe pulses; these can be displayed in the frequency domain by a Fourier transform with respect to t_1. Tanimura and Mukamel have proposed an off-resonant two-dimensional (2D) stimulated fifth-order Raman scattering experiment with two pump pulses followed by a probe.[24] The 2D stimulated Raman signal is displayed by double Fourier transform with respect to the two controlled time delays t_1 and t_2, and carries rich information about vibrations. UV pulses are under current development,[25–30] making multidimensional broadband UV resonant Raman experiments feasible.

We compare the spontaneous and stimulated 1D and 2D resonance Raman signals of L-tyrosine (Y), L-tryptophan (W), and the *trans*-L-tryptophan-L-tyrosine (WY) dipeptide (Fig. 1). The near UV spectra originate from the phenol (tyrosine) and indole (tryptophan) chromophores. There are two aromatic π–π^* electronic transitions above 210 nm in tyrosine and four in tryptophan.[31–33] Because vibrational modes are localized on specific chromophores, by using excitation pulses resonant with specific electronic transitions, the Raman peaks can often be assigned, even when their frequencies overlap. The correlation between vibrational modes localized at different groups in the WY dipeptide in 2DSRR spectra is examined by appropriate pulse configurations. The 2D technique is also superior to spontaneous Raman in distinguishing W/Y mixture and WY dipeptide.

Spontaneous and stimulated time-domain multipulse resonance Raman signals are described in the second section. Computational details are given in the third section. Simulation results are presented in the fourth through seventh sections, and we conclude in the last section.

* *Correspondence to: Shaul Mukamel, Department of Chemistry, University of California, Irvine, CA 92697, USA.*
E-mail: smukamel@uci.edu

Department of Chemistry, University of California, Irvine, CA, 92697, USA

Journal of RAMAN SPECTROSCOPY

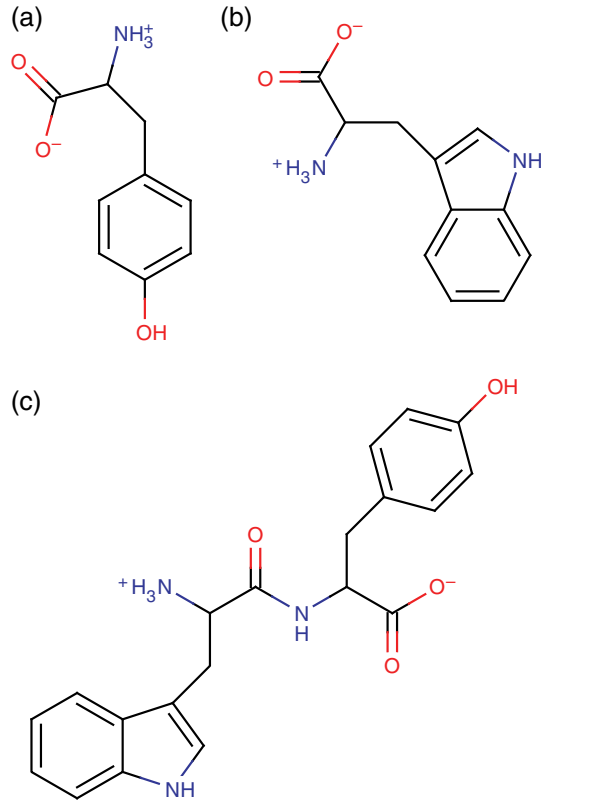

Figure 1. Structure of (a) tyrosine, (b) tryptophan, and (c) trans-Trp–Tyr (WY) dipeptide.

Theory

UV absorption

We assume a linearly displaced two-state harmonic vibrational Hamiltonian,

$$H = |g\rangle H_g \langle g| + \sum_e |e\rangle H_e \langle e| \tag{1}$$

with

$$\begin{aligned} H_g &= \sum_j \frac{1}{2}\omega_j \left(p_j^2 + q_j^2\right) \\ H_e &= \varepsilon_e + \sum_j \frac{1}{2}\omega_j \left(p_j^2 + \left(q_j + \Delta_j^e\right)^2\right) \end{aligned} \tag{2}$$

Here, q_j and p_j are the dimensionless coordinate and momentum of the jth normal mode, ε_e is the excitation energy of electronic state $|e\rangle$, and Δ_j^e is the dimensionless displacement. The displacements were evaluated by using the excited state gradient method.[11,34,35] The UV absorption spectra were calculated using the cumulant expression,[2]

$$\sigma_a(\omega) = \frac{1}{\pi}\Re \int_0^\infty dt\, exp\left[i(\omega - \omega_{eg})t - g(t) - \Gamma t\right] \tag{3}$$

where the line broadening function and electronic excitation energy are given by

$$g(t) = \sum_{e,j} \frac{\left(\Delta_e^j\right)^2}{2}\left\{\coth\left(\frac{\beta\omega_j}{2}\right)\left[1 - \cos(\omega_j t)\right] + i\left[\sin(\omega_j t) - \omega_j t\right]\right\} \tag{4}$$

$$\omega_{eg} = \varepsilon_e + \frac{1}{2}\sum_j \omega_j \left(\Delta_e^j\right)^2 \tag{5}$$

Here, $\beta = 1/k_B T$ is the inverse temperature and k_B is the Boltzmann constant. We used $T = 300$ K and electronic linewidth $\Gamma = 100\ cm^{-1}$.

Spontaneous resonance Raman

The spontaneous Raman signal is given by the Kramers–Heisenberg formula,

$$S^{SP}(\omega_1, \omega_2) = \sum_{c,a} P(a)\left|\alpha_{ca}(\omega_1)\right|^2 \delta(\omega_1 - \omega_2 - \omega_{ca}) \tag{6}$$

where ω_1 and ω_2 are the incident and signal frequencies, respectively, $|c\rangle$ and $|a\rangle$ are the final and initial vibrational states in the ground electronic state, and $P(a)$ is the population of state $|a\rangle$. The transition polarizability α is given by summing over intermediate vibronic states $|b\rangle$:

$$\alpha_{ca}(\omega_1) = \sum_b \frac{\langle c|\hat{\mu}|b\rangle\langle b|\hat{\mu}|a\rangle}{\omega_{ca} - \omega_1 - i\Gamma_b} \tag{7}$$

The number of relevant vibronic states increases exponentially with the number of vibrational modes. We have avoided these summations by using a multimode expression for resonance Raman signals based on the cumulant expansion for linearly displaced harmonic vibrations given in Appendix A. We have added a vibrational linewidth $\Gamma_{ca} = 10\ cm^{-1}$ to the delta function $\delta(\omega_1 - \omega_2 - \omega_{ca})$.

Selection of the stimulated resonance Raman signal

The impulsive pump probe signal that employs two pulses separated by a delay t_1 contains both ground state and excited state contributions as shown in the loop diagrams in Fig. 2. These diagrams provide a compact representation of the time evolution of the wavefunction, which contributes to the nonlinear signal, in much the same way that the ladder diagrams[2] represent the density-matrix evolution. In the loop diagrams, time flows clockwise from the bottom left to the bottom right, with forward (ket) evolution on the left branch and backward (bra) evolution on the right branch. Arrows pointing to (away from) the loop represent absorption (emission). Diagram rules can be found in the work of Biggs *et al.*[36] We are interested in diagrams I and II, which represent stimulated Raman scattering (SRS), where the pump interacts twice in an up-and-down fashion, creating a vibrational coherence. In the excited state contributions (diagrams III and IV), the pump pulse creates a vibrational wave packet in the excited electronic state in both the ket and the bra. The coherence between these wave packets can then be probed via a down-and-up transition, in a process known as excited state stimulated emission (diagram III). The probe can further induce an up-and-down transition to a doubly excited state, giving rise to excited state absorption (diagram IV).

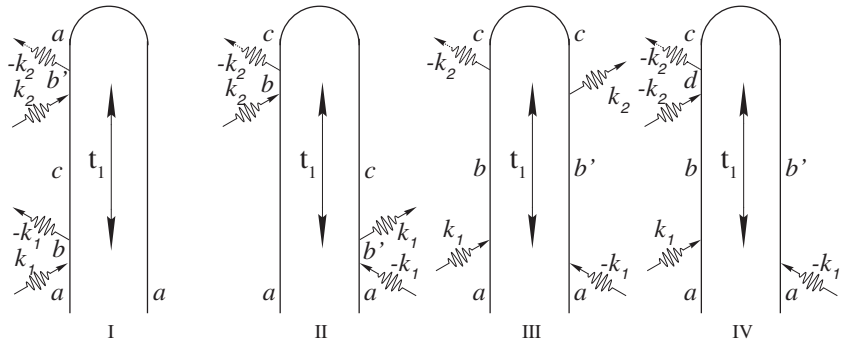

Figure 2. The four loop diagrams for the pump–probe experiment with well-separated pulses. Diagrams I and II represent stimulated resonance Raman, III is excited state stimulated emission, and IV is excited state absorption.

The Fourier transformed signal

$$S(\Omega) = \int_0^\infty dt_1 S(t_1) e^{i\Omega t_1} \tag{8}$$

will show peaks corresponding to the difference in energy between the ground state and the vibrationally excited states, i.e. fundamental, overtone, and combination bands. The SRS signals are easy to interpret because they only depend on ground state frequencies and are not affected by the complex photochemical and photophysical nonadiabatic processes that occur in UV excited states. For applications as markers to protein structure, it is therefore desirable to eliminate the excited state contributions and isolate the SRS signal. This will be discussed in the following.

The excited state contributions can be eliminated by using electronically off-resonant pump and probe pulses. However, in this case, we lose the selectivity of the resonance Raman process. To a given chromophore, if the excited electronic state has a very short (radiative or nonradiative) lifetime, any electronically excited population created by the pump will have decayed before the arrival of the probe and will therefore not contribute to the signal; we can then select the SRS diagrams. For example, the Soret excited states in heme-containing molecules have lifetimes of tens of femtoseconds, and any long-lived vibrational coherence detected at this excitation window can be attributed solely to the ground electronic state.[17] This is also the case in stimulated X-ray Raman spectroscopy,[37] which involve core transitions with very short (~10 fs) lifetimes.[38] This does not apply to tyrosine or tryptophan, which have long electronic lifetimes (≤10 ns).[39]

We shall discriminate against the excited state contributions, by using the fact that the excited state population decays much more rapidly with detuning than the ground state contribution. We show in Appendix B that for Gaussian pulses, the excited state contribution will vary as $exp(-d^2)$, with the effective detuning $d \equiv \sigma(\Omega - \omega_{eg})$, where Ω is the pulse center frequency and ω_{eg} is the excitation energy, while the SRS contribution varies as $1/d$. It is therefore possible to isolate the SRS signal by tuning the pump pulse to the *pre-resonant* region while keeping the resonant enhancement by a resonant probe. This strategy is easily extended to 2D by making both pumps pre-resonant. It is also possible to enhance the excited state stimulated emission contribution over the SRS and excited state absorption by using resonant pump and red-shifted probe.

One-dimensional stimulated resonance Raman (1DSRR)

The stimulated Raman signal represented by diagrams I and II of Fig. 2 is given by,[37]

$$S(t_1) = \Re\left[\left\langle \alpha^{(1)}(0)\alpha^{(2)}(t_1)\right\rangle - \left\langle \left(\alpha^{(1)}(0)\right)^\dagger \alpha^{(2)}(t_1)\right\rangle\right] \tag{9}$$

where the effective polarizability due to the nth pulse is

$$\begin{aligned}\alpha^{(n)}_{c'c} &\equiv \left\langle c'\left|\hat{\alpha}^{(n)}\right|c\right\rangle \\ &= \frac{1}{2\pi}\sum_b \left\langle c'\middle|b\right\rangle\left\langle b\middle|c\right\rangle\left|\mu_{eg}\right|^2 \int_{-\infty}^{\infty} d\omega \frac{E_n^*(\omega)E_n(\omega+\omega_{c'c})}{\omega+\omega_n-\omega_{bc'}+i\Gamma_b}\end{aligned} \tag{10}$$

where $|c\rangle$ and $|c'\rangle$ are vibrational eigenstates in the ground electronic state. $\hat{\alpha}^{(n)}$ is a non-Hermitian operator in the vibrational subspace, it becomes real Hermitian far off-resonance, where Eqn (9) reduces to a commutator.[40] The signal is recorded versus the pump-probe delay and Fourier transformed (Eqn (8)) giving the 1DSRR signal,

$$S(\Omega_1) = \sum_{ac} P(a) \frac{i\alpha^{(1)}_{ca}\left[\alpha^{(3)}_{ac} - \left(\alpha^{(3)}_{ac}\right)^*\right]}{\Omega_1 - \omega_{ca} + i\Gamma} . \tag{11}$$

As this is a pump-probe signal, and only the real part of Eqn(9) contributes, the Fourier transform signal obeys $S(-\Omega) = S^*(\Omega)$.

Two-dimensional stimulated resonance Raman (2DSRR)

The 2D stimulated Raman signal is obtained by adding a second pump, resulting in the three-pulse pump–pump–probe configurations shown in Fig. 3. The first pulse creates a vibrational excitation in either the ket (S_i and S_{iv}) or the bra (S_{ii} and S_{iii}). The second pulse can either create another pure vibrational excitation on the opposite side of the density matrix (S_i and S_{iii}) or change the excitation created by the first (S_{ii} and S_{iv}).

The 2D signal is written in the time domain as

$$\begin{aligned}S^{2DSRR}(t_1,t_2) &\equiv S_i + S_{ii} + S_{iii} + S_{iv} \\ &= -\Im\left[\left\langle \alpha^{(2)^\dagger}(t_{(1)})\alpha^{(3)}(t_2+t_1)\alpha^{(1)}(0)\right\rangle\right. \\ &\quad -\left\langle \alpha^{(1)^\dagger}(0)\alpha^{(2)^\dagger}(t_1)\alpha^{(3)}(t_2+t_1)\right\rangle \\ &\quad +\left\langle \alpha^{(1)^\dagger}(0)\alpha^{(3)}(t_2+t_1)\alpha^{(2)}(t_1)\right\rangle \\ &\quad \left.-\left\langle \alpha^{(3)}(t_2+t_1)\alpha^{(2)}(t_1)\alpha^{(1)}(0)\right\rangle\right]\end{aligned} \tag{12}$$

It will be displayed as frequency–frequency correlation plots obtained by a double Fourier transform:

Journal of RAMAN SPECTROSCOPY

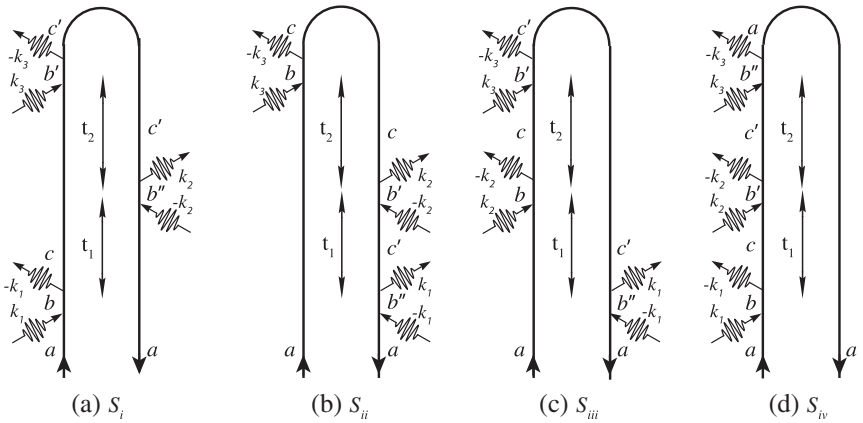

Figure 3. Loop diagrams for the 2D Raman signal: (a) S_i, (b) S_{ii}, (c) S_{iii}, and (d) S_{iv}.

$$S^{2DSRR}(\Omega_1,\Omega_2) = \int_0^\infty dt_1 \int_0^\infty dt_2 \exp(i\Omega_1 t_1 + i\Omega_2 t_2) S^{2DSRR}(t_1,t_2) = \sum_{acc'} \frac{P(a)\alpha_{ca}^{(1)}}{\Omega_1 - \omega_{ca} + i\Gamma} \left(\frac{\left(\alpha_{ac'}^{(2)}\right)^* \left[\alpha_{c'c}^{(3)} - \left(\alpha_{c'c}^{(3)}\right)^*\right]}{\Omega_2 - \omega_{cc'} + i\Gamma} - \frac{\alpha_{c'c}^{(2)} \left[\alpha_{ac'}^{(3)} - \left(\alpha_{ac'}^{(3)}\right)^*\right]}{\Omega_2 - \omega_{c'a} + i\Gamma} \right) . \quad (13)$$

The signal for negative $\Omega 1$ can be found by $S(-\Omega 1, -\Omega 2) = S^*(\Omega 1, \Omega 2)$.

Computational details

We used the Gaussian 09[41] package with time-dependent density functional theory, the PBE0 functional,[42,43] and 6-311++G(d,p) basis set in the calculations. The geometry was optimized to minimize its ground state energy; excited state gradients and displacements were calculated at that geometry. The conductor-like polarizable continuum model[44,45] was used to perform the self-consistent reaction field calculations in the aqueous environment. To correct for the systematic error in the density functional frequency calculations, we scaled all vibrational frequencies by a factor of 0.97.[46,47] Gaussian pulses envelopes with 1768 cm^{-1} (8.33 fs) full width at half maximum (FWHM) were used. This width covers a substantial region of the absorption spectrum as shown in Fig. 11 (c,d).

UV absorption spectra

To avoid overlap with the peptide n–π^* and π–π^* transitions, we focus on the electronic aromatic π–π^* transitions below 47 620 cm^{-1} (≥210 nm). The calculated dipole-allowed electronic excitations are given in Table 1. Using Platt's notation[48] for benzene electronic excitations, we assigned the two excited states of tyrosine at 251 and 222 nm as L_b and L_a, respectively. These transition dipole moments are perpendicular. The 268 and 253 nm peaks of tryptophan are assigned as L_b and L_a transitions, and the Trp–B_b transition is split into two peaks because the D_{6h} symmetry is broken. The Trp–B_a transition lies below 200 nm. The two Tyr transitions and the four Trp transitions are present in the dipeptide, with slight shifts due to the change of chemical environments of each aromatic group. The natural transition orbitals (NTO)[49] of the electronic transitions presented in Figs S1–S3 (Supporting Information) show that the hole (left) and electron (right) states are localized on the aromatic groups.

The calculated electronic excitations of tyrosine (Y), tryptophan (W), 1:1 W/Y mixture, and WY dipeptide in aqueous solution are compared with experimental absorption spectra in Fig. 4. Spectra of the mixture are obtained by adding the tyrosine and

Table 1. UV electronic transitions (≥210 nm) of tyrosine, tryptophan, and trans-WY dipeptide

System	Excitation	λ (nm)	$\tilde{\nu}$ (cm^{-1})	Dipole (debye) x	y	z	$\lvert\mu\rvert^2$	Description
Tyr		251	39 840	0.2591	0.8256	−0.0460	0.7509	L_b
		222	45 063	−1.4171	0.1179	0.4182	2.1970	L_a
Trp		268	37 228	0.5406	1.1506	−0.2523	1.6856	L_b
		253	39 484	-0.6788	0.6651	−0.3767	1.0450	L_a
		222	45 023	1.9159	−1.5794	0.8076	6.8160	B_b
		215	46 351	0.5879	−0.7750	0.5128	1.2092	B_b'
WYD	ε_1	270	37 015	0.2302	−0.2888	1.2589	1.7212	Trp–L_b ($\pi \rightarrow \pi^*$)
	ε_2	254	39 389	0.7973	−0.2485	0.0880	0.7051	Tyr–L_b ($\pi \rightarrow \pi^*$)
	ε_3	253	39 461	0.7478	−0.5153	0.0507	0.8272	Trp–L_a ($\pi \rightarrow \pi^*$)
	ε_4	232	42 976	−0.4976	−1.3340	0.5809	2.3646	Tyr–L_a ($\pi \rightarrow \pi^*$)
	ε_5	220	45 390	1.9180	−1.3655	0.2285	5.5959	Trp–B_b ($\pi \rightarrow \pi^*$)
	ε_6	218	45 827	−0.9231	0.4962	−0.1731	1.1282	Trp–B_b' ($\pi \rightarrow \pi^*$)

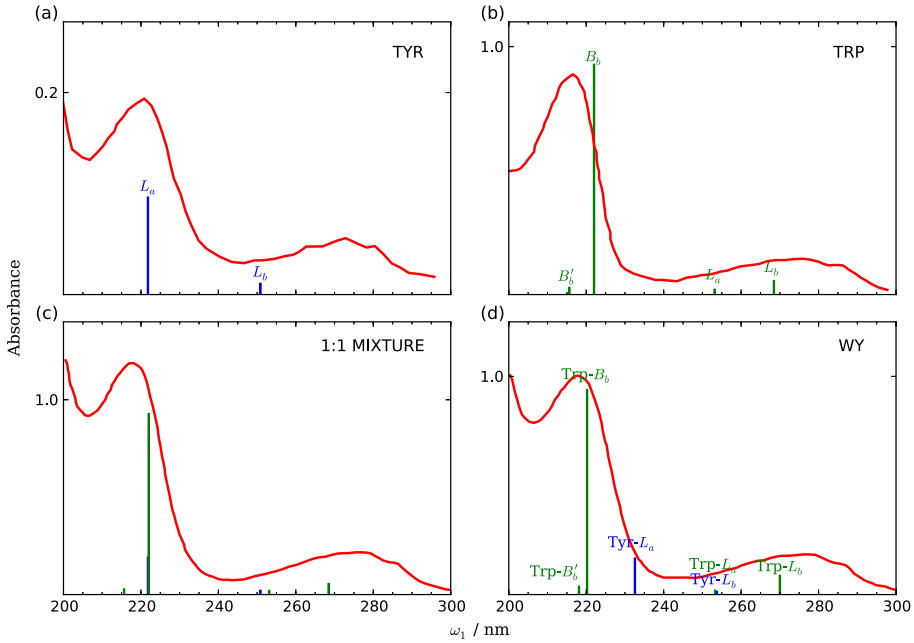

Figure 4. Experimental absorption spectra and calculated electronic stick spectrum of (a) tyrosine (blue), (b) tryptophan (green), (c) 1:1 mixture, and (d) WY dipeptide. The experimental spectra of tyrosine and tryptophan are taken from the work of Rava and Spiro.[32] The spectra of 1:1 mixture and dipeptide are taken from the work of Asher *et al.*[31] This figure is available in colour online at wileyonlinelibrary.com/journal/jrs.

tryptophan contributions. As shown in panels (a) and (b), both tyrosine and tryptophan have strong absorption at ∼220 and ∼270 nm. The ∼270 nm bands for both tyrosine and tryptophan are assigned as the L_b transitions. The ∼220 nm band is assigned as the L_a transition for tyrosine but as the B_b transition for tryptophan. The experimental absorption spectra of 1:1 W/Y mixture and WY dipeptide are very similar (red lines in panels (c) and (d)) and are dominated by two bands at 270 and 218 nm. The broad peak at 260–280 nm consists of the Trp–L_b, Trp–L_a, and Tyr–L_b transitions, and the peak centered at 220 nm consists of the Tyr–L_a and Trp–B_b transitions. The time-dependent density functional theory/PBE0 excitation energies of Trp–L_{ab} and Tyr–L_b bands are overestimated compared with those in the experiment.[50] The Tyr–L_a transition is red-shifted from 222 to 232 nm upon binding with tryptophan, resulting in a smaller splitting between Tyr–L_b and Tyr–L_a transitions. The splitting between Trp–B_b and Trp–B_b is also smaller in the dipeptide than in tryptophan monomer, which can be rationalized because the electronic states are more delocalized in the dipeptide.

Figure 5 shows the absorption spectra calculated using Eqn (3). For all the three systems, the main peak corresponding to each electronic excitation comes from the $|0^e\rangle \leftarrow |0^g\rangle$ transition. The tailing peaks in the high-frequency side of the main peaks correspond to $|1^e\rangle \leftarrow |0^g\rangle$ transitions for different vibrational modes. There is substantial overlap between different electronic transition contributions in the tryptophan and WY dipeptide. For instance, the splitting between the Trp–B_b and Trp–B_b transitions are 1328 and 427 cm^{-1} in tryptophan and WY, respectively, and are lower than the vibrational energy of the mode ν_{40} (W8b, 1588 cm^{-1}).

Spontaneous resonance Raman spectra

The 42 Raman active vibrational modes of WY are listed in Table 2. Almost all modes are localized either on the tryptophan (cyan) or on the tyrosine (magenta). Delocalized or peptide vibrational modes (uncolored) are expected to be resonantly enhanced by both Trp and Tyr transitions.

To benchmark our simulation protocol, we first compare our calculated spontaneous resonance Raman (SPRR) spectra (Eqn (6)) with that in the experiment. Figure 6 shows the experimental UVRR spectra of 1:1 W/Y mixture and WY dipeptide excited at 255 nm, which is resonant with the Trp–B_b and Tyr–L_a transitions.[31] The dominant peaks at 1555, 1350, 1015, and 760 cm^{-1} correspond to the totally symmetric Trp modes, and the 1610 cm^{-1} peak represents Tyr ring mode (Y20a[31,32]). The spontaneous UVRR spectra of W/Y mixture and WY dipeptide are very similar; it is difficult to distinguish different bonding patterns of systems containing tyrosine and tryptophan residues by using 225 nm spontaneous Raman. These are reproduced by our simulations. The contributions from tyrosine and tryptophan monomers are shown as dashed lines in Fig. 6(a). The 1610 cm^{-1} Y20a mode is predicted as 1628 cm^{-1}, as listed in Table 2. The calculated frequencies of active tryptophan modes are 1562, 1347, 1011, and 761 cm^{-1}, which can be assigned to ν_{39} pyrrole ring stretching, ν_{30} ring C–H/N–H bending, ν_{15} benzene ring symmetric breath, and ν_7 aromatic ring breath modes.

Two-dimensional plots of spontaneous Raman (2DSPR) spectra with respect to the excitation frequency (ω_1) and the Raman shift ($\omega_1 - \omega_2$) are shown in the left panel of Fig. 7 for excitation energies between 36 000 and 48 000 cm^{-1}. All 2D spectra in this article are displayed using the inverse hyperbolic sine function, which better reveals both weak and strong features:

$$\bar{S} = \text{arcsinh}(CS) \tag{14}$$

The normalization coefficient C is chosen to make $\bar{S}$ close to 1. Two horizontal slices are shown in Fig. 7(a,b). The vertical lines are Raman excitation profiles. The peaks along the tilted directions (dashed lines in Fig. 8(c,d)) in the 2DSPR correspond to the Raman signals enhanced by 0–1 vibronic excitations for each active mode.

Journal of RAMAN SPECTROSCOPY

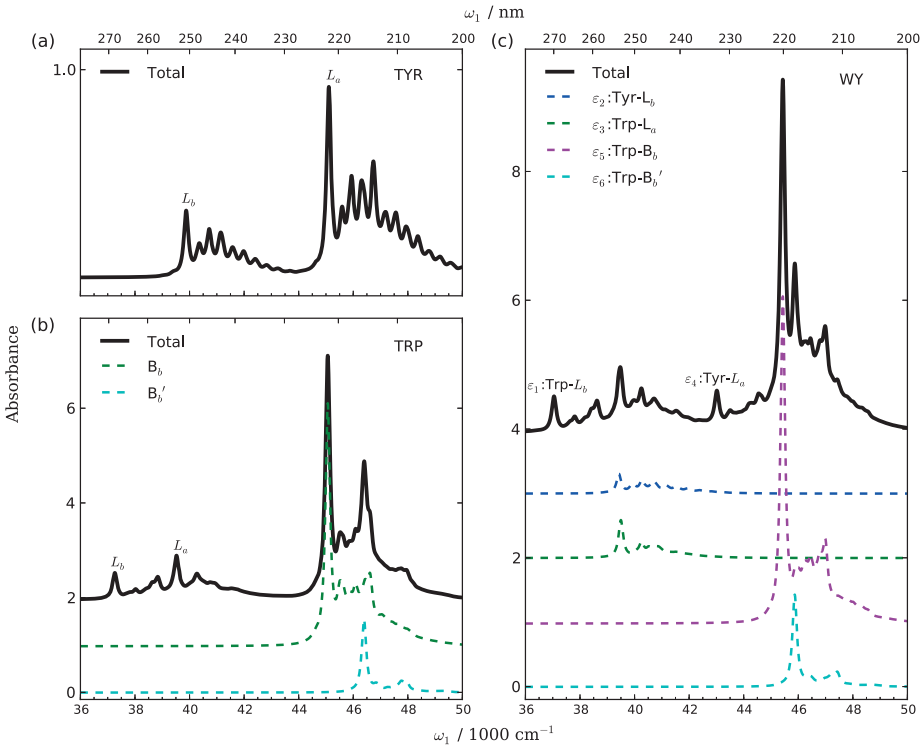

Figure 5. Simulated absorption spectra of (a) tyrosine, (b) tryptophan, and (c) trans-WY dipeptide in aqueous solution. Vibronic contributions are included by using the cumulant expansion. Overlapping electronic transitions are shown by dashed lines. An electronic linewidth $\Gamma = 100\,\mathrm{cm}^{-1}$ is used.

In Fig. 7, panels (a) and (b) display two horizontal slices of the 2DSPR spectra of *trans*-WY dipeptide corresponding to the 232 nm (ε_4:Tyr–L_a) and 270 nm (ε_1:Trp–L_b) resonances. The NTO plots of the dipole-allowed electronic transitions of the WY dipeptide (Fig. S3 (Supporting Information)) show that all the excitations are localized on either the Trp or the Tyr aromatic group; hence, the active vibrational modes enhanced by a resonant excitation should also be localized. This can be verified by examining the enhanced vibrational modes in a specific excitation. We assigned all the pronounced vibrational modes enhanced by the Tyr–L_a and Trp–B_b transitions, respectively. The assigned modes are listed in Table 2. Only ν_{13}, ν_{21}, and ν_{22} are enhanced by both transitions, reflecting their delocalized peptide bond nature. All other Raman signals are induced by vibrational modes localized on either the Tyr or the Trp aromatic group. The main features of tyrosine SPRR are the peaks at 1629 and 1510 cm^{-1}, which were assigned as the Y20a, Y19a, and Y18a phenol ring stretching modes.[31,32] The 780 and 850 cm^{-1} phenol ring breathing modes are not intense enough to characterize tyrosine residues. The tryptophan SPRR show peaks at 1590, 1360, 1125, and 760 cm^{-1}, which can be assigned as the W8b, W14, benzene ring H–C–C–H in-plane bending, and aromatic ring breath modes, respectively.[31,32] These resonance Raman signals are strong and have high selectivity upon excitations and thus can be used to characterize tyrosine and tryptophan residues.

Figure 8 compares the 2DSPR spectra of tyrosine, tryptophan, 1:1 W/Y mixture, and WY dipeptide. The spectra of tyrosine are much simpler than tryptophan and WY: there are only two electronic transitions in the range below 48 000 cm^{-1}, and the gap between these two excitations is 5200 cm^{-1}, which is much larger than any vibrational frequency. Thus, there is no overlap between peaks in the tilted direction from a lower excitation and horizontal peaks from a higher one. As the result of the smaller transition dipoles (Table 1), the Raman signals of tyrosine (Fig. 8(a)) are much weaker than those of tryptophan and WY dipeptide. The L_b and L_a transitions of tyrosine are close to the L_a and B_b transitions of tryptophan, and the SPRR of tyrosine excited with these wavelengths is overwhelmed by the contribution from tryptophan, which results in the fact that the spontaneous spectra of tryptophan (Fig. 8(b)) and 1:1 mixture (Fig. 8(c)) have similar patterns.

Despite the small differences between the spectra of the W/Y mixture and WY dipeptide at 225 nm (Fig. 6), it is possible to distinguish the two systems by the 2DSPR spectra. Below 41 500 cm^{-1}, the spectra of the two systems are similar, except for a slight shift. However, a series of horizontal peaks appear at 42,976 cm^{-1} in the dipeptide spectra (Fig. 8(d)), and its concomitant tilted peaks (blue dashed line) extend from 43 600 to 44 600 cm^{-1}, overlapping with the lower tail of the 45 390 cm^{-1} Trp–B_b horizontal peaks. This is a consequence of the red-shifted Tyr–L_a transition from 222 nm (45 023 cm^{-1}) in the tyrosine monomer to 232 nm (42 976 cm^{-1}) in the dipeptide. In addition, as the result of the shift of Trp–B_b and Trp–B_b transitions upon binding with tyrosine, the Raman profiles have an obvious shift as shown in the horizontal slices in Fig. 8.

1DSRR spectra

The modulus of the transition polarizability matrices (Eqn (7)) for different pulse frequencies are shown in Fig. 9. We used Gaussian UV pulses, with FWHM 1768 cm^{-1} (8.33 fs), and with center frequencies at 35 500, 37 015, and 42 976 cm^{-1}. The first pulse is chosen to be pre-resonant to Trp–L_b (ε_1), and the latter two frequencies are resonant with the Trp–L_b and Tyr–L_a (ε_4) transitions in WY dipeptide, respectively. The axes are labeled by

Table 2. Active vibrational modes in the range 600–1800 cm^{-1}. Cyan, magenta, and white rows represent vibration modes of trytophan (W), tyrosine (Y), and peptide bond. Aromatic ring modes labeling is from the works of Rava and Spiro[32,55]

Modes	Freq (cal., cm^{-1})	Description
ν_1	617.15	W ring out of plane deformation, Y peptide N-H bending
ν_2	650.95	Y peptide N–H bending
ν_3	735.86	W ring stretching, C–H out-of-plane bending
ν_4	743.18	W ring out-of-plane deformation, N–H bending
ν_5	753.08	W ring out-of-plane deformation
ν_6	758.52	Y C–C=O bending, C_α–H/N–H bending
ν_7	761.42	W ring breath
ν_8	776.40	Y Bz ring in-plane deformation, Bz–OH stretching
ν_9	814.05	Y Bz out-of-plane C–H bending (11)
ν_{10}	838.03	Y Bz out-of-plane C–H bending (11), C–C=O stretching
ν_{11}	846.84	Y Bz ring symmetric breath (1)
ν_{12}	865.98	W ring in-plane deformation
ν_{13}	881.02	peptide bending
ν_{14}	979.19	Y C_α–C=O stretching
ν_{15}	1010.75	W Bz ring symmetric breath
ν_{16}	1111.62	W Bz C–H bending
ν_{17}	1124.37	W Bz H–C–C–H scissor bending
ν_{18}	1138.82	W Bz H–C–C–H scissor bending
ν_{19}	1139.82	Y peptide C–H/C_α–H bending
ν_{20}	1154.96	Y Bz H–C–C–H scissor bending
ν_{21}	1181.47	peptide N–H bending
ν_{22}	1192.97	peptide N–H/C_α–H bending
ν_{23}	1229.56	W pyrrole ring deformation, pyrrole N–H bending
ν_{24}	1239.13	W ring ring C–H/N–H in-plane bending
ν_{25}	1253.95	Y Bz–OH stetching (20a)
ν_{26}	1266.77	Y 8a
ν_{27}	1281.21	Y peptide C–H bending
ν_{28}	1316.83	Y 3
ν_{29}	1327.06	W peptide C–H bending
ν_{30}	1347.49	W ring C–H/N–H bending
ν_{31}	1359.86	W 14
ν_{32}	1370.44	W C_α–H bending
ν_{33}	1382.96	Y peptide C–H bending, C–C=O stretching
ν_{34}	1425.18	W 6π
ν_{35}	1451.54	W 19b
ν_{36}	1488.75	W 19a
ν_{37}	1507.50	Y 19a
ν_{38}	1514.60	Y 18a
ν_{39}	1562.64	W pyrrole ring stretching
ν_{40}	1588.43	W 8b
ν_{41}	1590.35	W NH3 bending, ring stretching
ν_{42}	1628.72	Y 20a

Journal of RAMAN SPECTROSCOPY

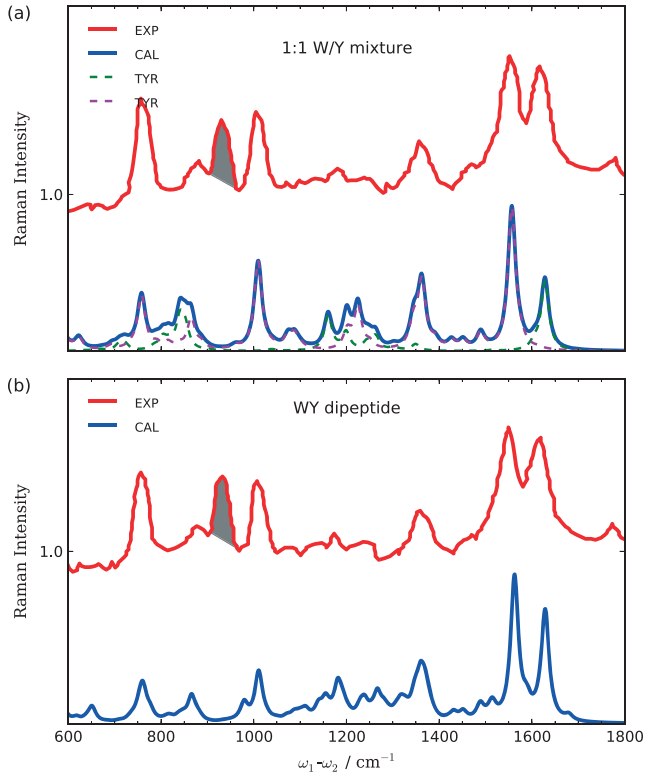

Figure 6. Comparison between experimental (red) and calculated (blue) spontaneous resonance Raman spectra of (a) 1:1 tyrosine/tryptophan mixture and (b) WY dipeptide excited at 225 nm (44 444 cm^{-1}). Experimental data are taken from the work of Rava and Spiro.[31] Contributions from solvent modes are shaded in the experimental spectra. The calculated spectra of 1:1 mixture are obtained by summing the spectra of tyrosine (green dashed) and tryptophan (magenta dashed). The shaded peaks at 932 cm^{-1} come from internal standard. This figure is available in colour online at wileyonlinelibrary.com/journal/jrs.

the active vibrational modes listed in Table 2. The matrix elements of the polarizability due to the *n*th pulse can be written as

$$\alpha_{ji}^{(n)} = {}_0\left\langle (0)_g^i (1)_g^j \middle| \hat{\alpha}^{(n)} \middle| (1)_g^i (0)_g^j \right\rangle_0 \tag{15}$$

which can be viewed as the transition amplitude between two vibrational modes; hence, the α matrix is symmetric.

The top row of the α matrix is the only contribution to the spontaneous and 1DSRR signals, as each transition must be between the ground state and a vibrationally excited state. The largest values of α are found along the diagonal, where the initial and final states are the same (elastic scattering). For 1DSRR, the diagonal element α_{00} contributes to the elastic scattering background term that we do not include in our simulations. The $\alpha^{(0)}$ and $\alpha^{(1)}$ matrices in Fig. 9(a,b) exhibit block-wise behaviors, where the elements between tryptophan modes, such as ν_7, ν_{16-18}, ν_{29-36}, and ν_{39-41} (Table 2) have larger values than the others, as a consequence of the excitation beam being near resonance or on resonance with the Trp–L_b transition. The transition polarizability matrices can be better visualized by regrouping the vibrational modes into tryptophan, tyrosine, and peptide modes, as shown Fig. 10. In panels (a) and (b), it is obvious that off-diagonal terms corresponding to vibrational modes from tryptophan (Trp–Trp, upper left bright block) have larger values than those involved modes from both tryptophan and tyrosine (Trp–Tyr and Tyr–Trp dark blocks). The bright rectangular Pep–Trp (lower left) and Trp–Pep (upper right) blocks in panels (a) and (b) show the transition polarizabilities between peptide and tryptophan modes. Because the peptide bond modes are delocalized, these off-diagonal terms have larger values that indicate strong correlation. The correlation between tyrosine modes with others are weak because no tyrosine electronic transitions can be excited by using pulses centered at $\omega_1 = \varepsilon_0 = 35\,500$ cm^{-1} (panel (a), pre-resonant) or $\omega_1 = \varepsilon_1 = 37\,015$ cm^{-1} (panel (b), resonant with Trp–L_b). On the other hand, in Fig. 10 (c), as shown in the top panel, although the excitation beam is

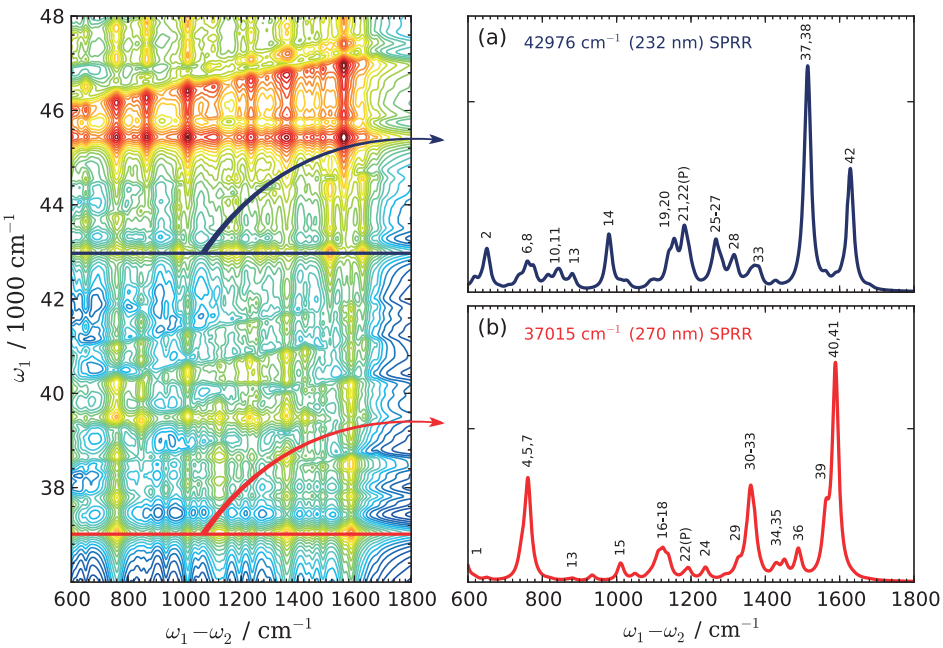

Figure 7. (Left) Two-dimensional spontaneous Raman spectra of WY dipeptide with excitation energy scanned from 36 000 to 48 000 cm^{-1}. Horizontal slices excited at (a) $\omega_1 = 232$ nm and (b) $\omega_1 = 270$ nm, respectively. Vibrational mode assignment as listed in Table 2. A nonlinear scale function (Eqn (14)) is used for better visibility. SPRR, spontaneous resonance Raman.

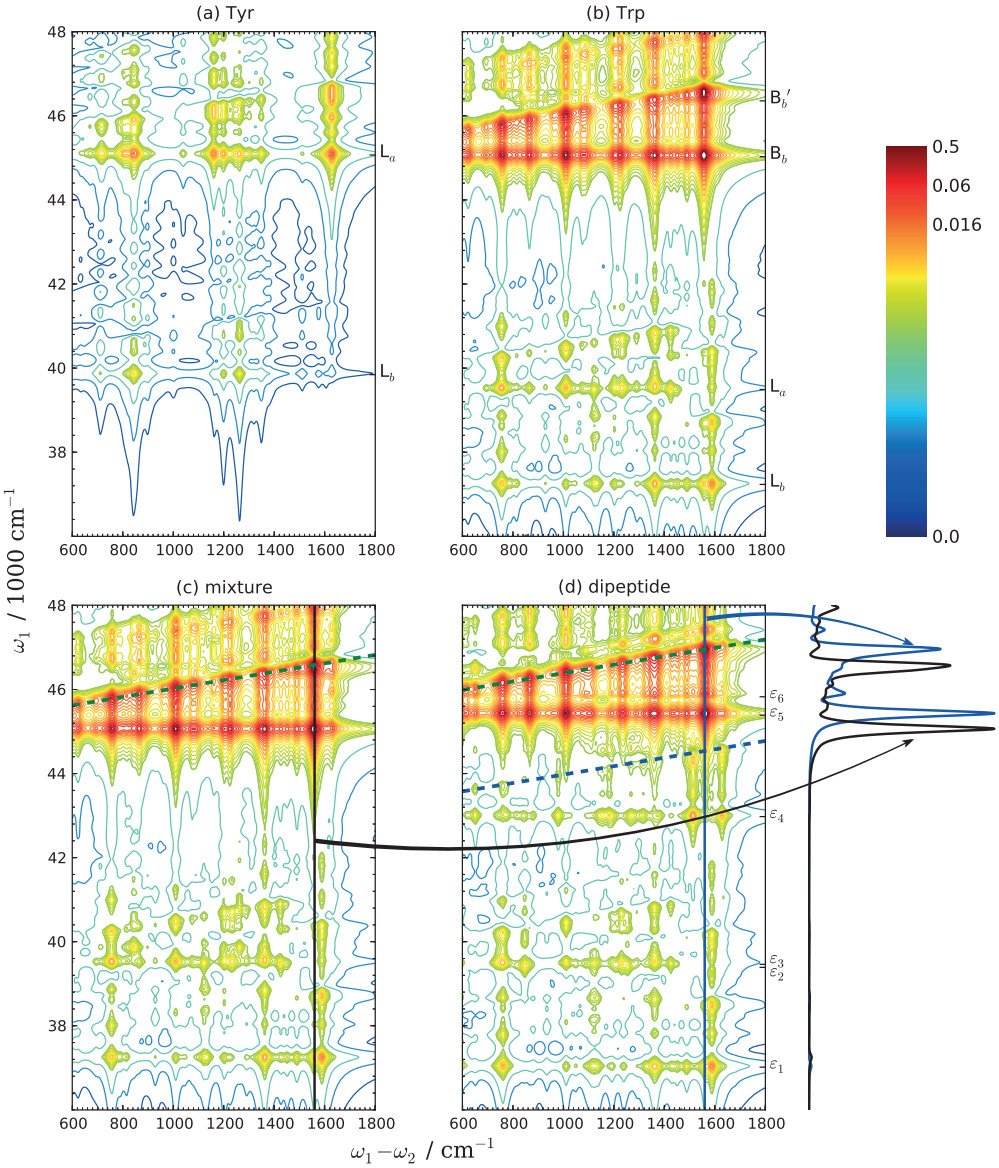

Figure 8. Two-dimensional spontaneous Raman spectra of (a) tyrosine, (b) tryptophan, (c) 1:1 mixture, and (d) WY dipeptide. The spectra of mixture are obtained by summing the contributions from tyrosine and tryptophan. Vertical slices of the mixture and dipeptide spectra show a shift between Raman profile peaks of (c, black) and (d, blue). Dashed lines denote the tilted directions. A nonlinear scale function (Eqn (14)) is used for better visibility. This figure is available in colour online at wileyonlinelibrary.com/journal/jrs.

resonant with the Tyr–L_a transition, there is considerable overlaps between the excitation pulse with the upper tail of the Trp–L_a and the lower tail of the Trp–B_b transitions; thus, both tyrosine and tryptophan modes can be enhanced by the broadband pulse centered at ε_4 (Fig. 9(c)). The simultaneous excitation of tryptophan and tyrosine transitions results in strong correlations between tyrosine modes with the others, which can be visualized by the off-diagonal Trp–Tyr and Tyr–Trp blocks in panel (c).

The SPRR and time-domain 1DSRR spectra are compared in Fig. 11. In the 1DSRR experiment, the system is first pumped with a pre-resonant pulse centered at ε_0:35 500 cm^{-1} and then detected by a probe pulse with center frequency resonant with the ε_1:Trp–L_b (Fig. 11(c)) or the ε_4:Tyr–L_a (Fig. 11(d)) transition. The absorption spectra and pulse spectral density are given in the insets in Fig. 11(c,d). The 1DSRR spectrum with $\omega_1 = \varepsilon_0$ and $\omega_2 = \varepsilon_1$ reproduces all the characteristic features of the tryptophan aromatic modes at 1590, 1360, 1125, and 760 cm^{-1}. However, in the case of $\omega_1 = \varepsilon_0$ and $\omega_2 = \varepsilon_4$, in addition to the characteristic features of the tyrosine aromatic modes at 1629 and 1510 cm^{-1}, tryptophan modes at 1590, 1360, and 760 cm^{-1} are also enhanced. The contribution from tryptophan is a result of the excitation of Trp–L_b by ε_0 and Trp–L_a/Trp–B_b by ε_4, as shown in the insert of Fig. 11(d).

2DSRR spectra

The 2DSRR signals are written as the product of two top row elements $\alpha_{ac'}$ and α_{ca} with an intermediate term $\alpha_{c'c}$. Peaks along Ω_1 occur at the same frequencies as in the spontaneous and 1DSRR signals, whereas Ω_2 peaks can occur either at these frequencies (S_{ii} and S_{iv}) or at the difference between vibrational frequencies (S_i and S_{iii}). The intermediate term $\alpha_{cc'}$ probes the polarizability matrix element between different vibrational modes, and it thus carries additional information about the intermediate Raman process between these modes, which is not available in the 1D signals.

Journal of RAMAN SPECTROSCOPY

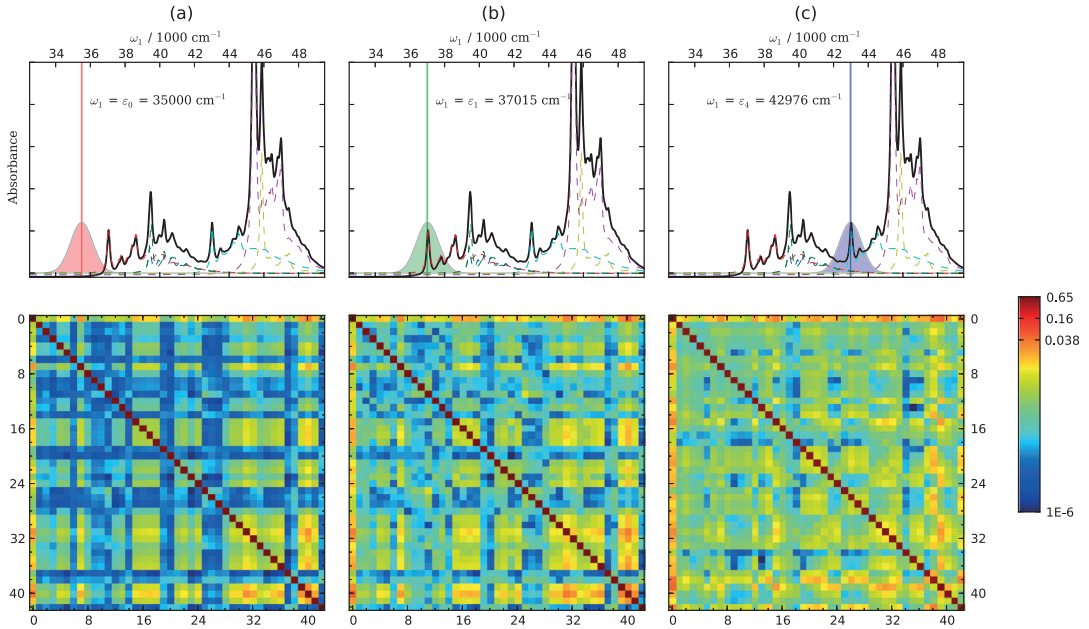

Figure 9. Modulus of transition polarizability matrices (Eqn (15)) for (a) ε_0 35 500 cm^{-1}, (b) ε_1:Trp–L$_b$ 37015 cm^{-1}, and (c) ε_4:Tyr–L$_a$ 42 976 cm^{-1}. Pulses and the absorption spectra are shown on top. Axes of the matrices are labeled by the vibrational modes as listed in Table 2, and v_0 is the ground vibrational state. Log scale function $\bar{\alpha} = log(\alpha)$ is used for better visibility. This figure is available in colour online at wileyonlinelibrary.com/journal/jrs.

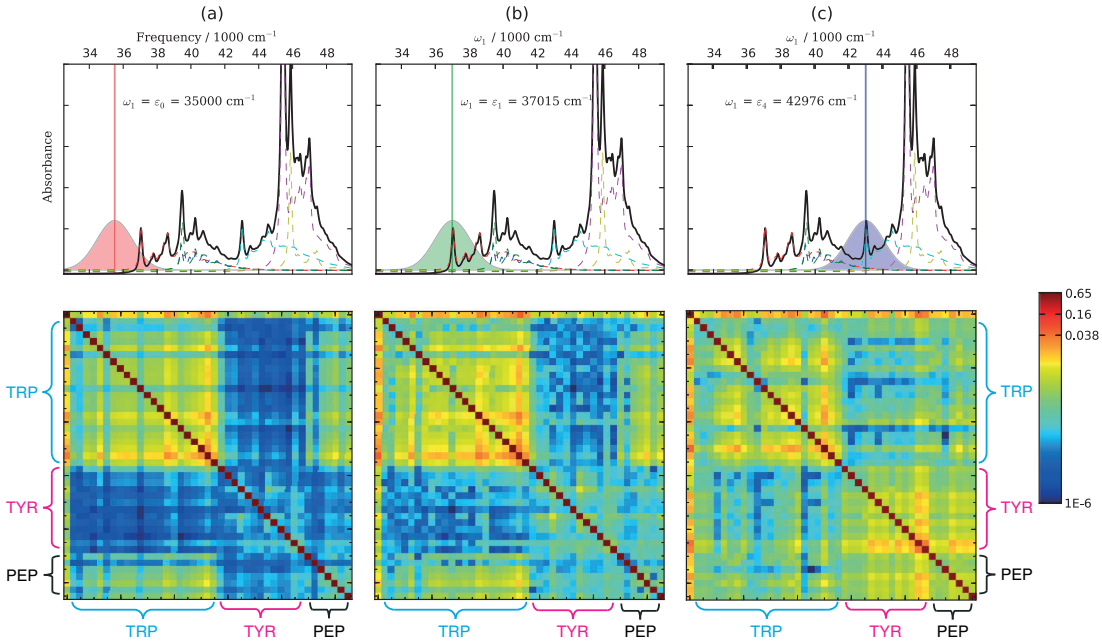

Figure 10. Same as Figure 9 except that vibrational modes are regrouped: Mode 0 denotes ground state, and the first 22, the 23th–35th, and the 36th–42nd modes are Trp (tryptophan), Tyr (tyrosine), and Pep (peptide) modes, respectively. This figure is available in colour online at wileyonlinelibrary.com/journal/jrs.

The 2DSRR spectra reveal the correlation between different vibrational modes. In Fig. 12, we show the 2D spectrum for $\omega_1 = \omega_2 = \varepsilon_0$ and $\omega_3 = \varepsilon_1$. Because the 2D signals have inversion symmetry,[52] only the $\Omega_1 > 0$ region is displayed. The time-independent contribution that all three Raman processes are 0–0 elastic scattering is filtered out. Various slices along the diagonal and horizontal directions are shown in the middle column. The diagonal trace is similar to the 1DSRR spectrum (Fig. 11(c)) with narrower line shapes. A horizontal trace, with a constant $\Omega_2 = 1588\,\text{cm}^{-1}$ corresponding to the v_{40} W8b mode listed in Table 2 is also shown in Fig. 12(a). The same diagonal peak with coordinate $(\Omega_1, \Omega_2) = (1588, 1588)\,\text{cm}^{-1}$ appears in Fig. 12(a,b). It consists of contributions from pathways S_i and S_{iv}, as shown in the right column, with values proportional to $\left(\alpha_{00}^{(0)}\right)^* \left(\alpha_{0,40}^{(0)}\right)\left(\alpha_{40,0}^{(0)}\right)$ and $\left(\alpha_{0,40}^{(1)}\right)\left(\alpha_{40,40}^{(0)}\right)\left(\alpha_{40,0}^{(0)}\right)$, respectively. Diagonal peaks are the strongest features in the 2D spectra because it contains a diagonal element of α. For pathways S_i and S_{iii}, a diagonal peak arises from $a = c'$ or $a = c$. Likewise in S_{ii} and S_{iv}, diagonal peaks are the results of elastic process with $c = c'$.

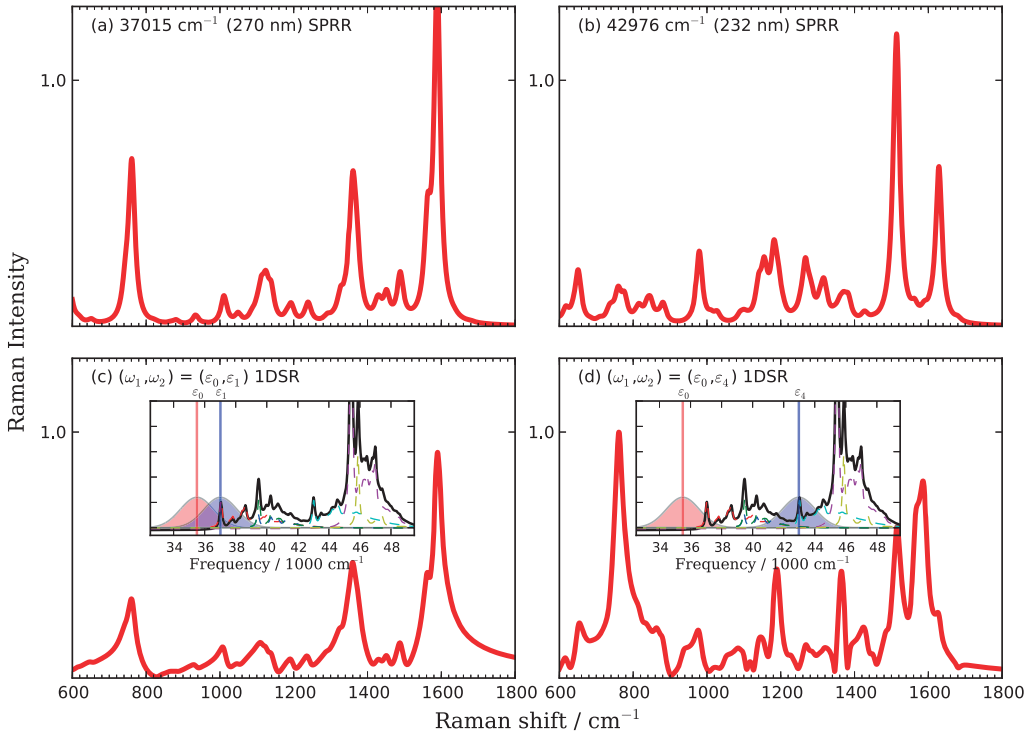

Figure 11. Spontaneous resonance Raman (SPRR) spectra of WY dipeptide calculated at ω_1 resonant with (a) ε_1:Trp–L_b and (b) ε_4:Tyr–L_a. One-dimensional stimulated resonance Raman (1DSRR) spectra calculated for a pre-resonant pulse ($\omega_1 = 35\,500\,\text{cm}^{-1}$) as pump and probe pulse resonant with (c) ε_1 and (d) ε_4. Pulses are shown in the inserts.

When two different vibrational modes are involved, off-diagonal peaks of two different diversities appear. S_{ii} and S_{iv} contain peaks at $(\Omega_1,\Omega_2) = (\pm\omega_{ca}, \pm\omega c' a)$, i.e. both Ω_1 and Ω_2 correspond to a $\left|(1)_g\right\rangle_0 \leftarrow \left|(0)_g\right\rangle$ transition with different modes. In the other pathways, $\Omega_2 = \pm\omega_{cc'}$ is the difference between two vibrational excitations. For instance, the 1360 cm^{-1} peak in Fig. 12(a) has intensity proportional to $\left(\alpha^{(1)}_{0,40}\right)\left(\alpha^{(0)}_{40,31}\right)\left(\alpha^{(0)}_{31,0}\right)$, different from the diagonal peaks, where one top row, one diagonal, and the 0–0 transition polarizability matrix elements account. For the off-diagonal peaks, two different top rows and one off-diagonal elements affect the intensity. The fact that the off-diagonal peak intensities are one order of magnitude weaker than those of the diagonal ones indicates that the intermode correlation between different vibrational modes is one order of magnitude weaker than the elastic scattering 1–1 transition (Fig. 12(b,c)). The 1360 cm^{-1} peak in Fig. 12(d) has a coordinate (ν_{31}, $\nu_{31} - \nu_{40}$) in the 2DSRR spectrum, which is proportional to the amplitude $\left(\alpha^{(0)}_{0,40}\right)^*\left(\alpha^{(1)}_{40,31}\right)\left(\alpha^{(0)}_{31,0}\right)$. It also reflects the intermode correlation. The intermode correlation arises from the process that one vibrational quantum transfers from one mode to another via an electronic excitation. A strong correlation implies that the electronic transition is strongly coupled to the two different modes. In the current study, because all the electronic transitions are localized on aromatic groups, only vibrational modes from the same group are strongly correlated.

The modulus of 2DSRR signals of tyrosine, tryptophan, 1:1 W/Y mixture, and WY dipeptide are shown in Fig. 13 for $\omega_1 = \omega_2 = \varepsilon_0$ and $\omega_3 = \varepsilon_1$. When the probe pulse is resonant with ε_1:Trp–L_b, there is little differences between the 2DSRR spectra of the W/Y mixture and WY dipeptide, and the contribution from the tyrosine to the mixture spectra is negligible. This can be attributed to the fact that there is no electronic excitation in the tyrosine monomer resonant with any incident pulses; thus, no Raman process would be enhanced during the measurement. The situation is almost the same for the tyrosine residue in WY dipeptide; the tyrosine-related excitations lie far away from the pulse frequencies, and only tryptophan modes can be significantly enhanced.

The situation is different when the probe is resonant with ε_4: Tyr–L_a as shown in Fig. 14 for $\omega_1 = \omega_2 = \varepsilon_0$ and $\omega_3 = \varepsilon_4$. Both tyrosine and tryptophan monomers have strong Raman signals and exhibit their characteristic vibrational modes on the diagonal lines. This is the result of the fact that ε_4 lies near the L_a transition in tyrosine and the B_b transition in tryptophan, respectively. We can also see the stronger intermode correlation of tryptophan indicated by the cross peaks in Fig. 14(b) compared with those in Fig. 14(a). For the WY spectrum shown in Fig. 14(d), only the tyrosine mode ν_6 and tryptophan mode ν_{40}, which are the strongest features in the monomer spectra, are prominent in the dipeptide spectra. All other features in the range 1100–1400 cm^{-1} have much weaker intensities than ν_6 and ν_{40}. The weaker signals in the WY spectrum is a consequence of the relatively delocalization of electrons in the dimer compared with that in the monomers. The delocalized electronic states result in smaller dimensionless displacements between the excited and ground state minimums. The values of the dimensionless displacements of the monomers and dimer can be found in Tables S1–S3 (Supporting Information). For instance, the displacements for the tryptophan W14 mode (ν_{31}) corresponding the Trp–L_b transition are 0.713 and 0.576 in tryptophan monomer and dimer, respectively. The evident differences between the 2D spectra of monomer mixture and dimer indicates that by choosing appropriate pulse configurations, 2DSRR technique can facilitate the distinction of systems with similar chemical compositions but with different bonding interactions.

Journal of RAMAN SPECTROSCOPY

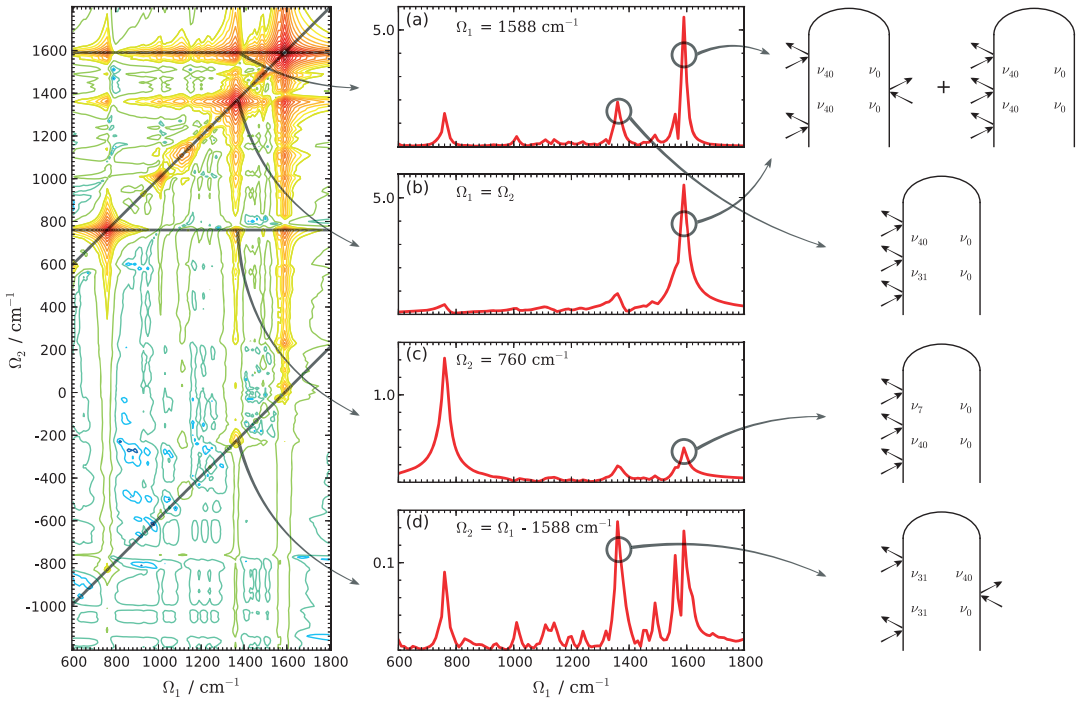

Figure 12. (a) Simulated two-dimensional stimulated resonance Raman spectra of the WY dipeptide with $\omega_1 = \omega_2 = \varepsilon_0$ and $\omega_3 = \varepsilon_1$. (a,d) Diagonal and (b,c) horizontal slices of the two-dimensional spectrum on the left. (Right) Loop diagrams corresponding to selected peaks.

Conclusions

We have simulated the 1D and 2D broadband stimulated UVRR spectra. The correlations between vibrational modes enhanced by UV pulses are illustrated for L-tyrosine, L-tryptophan, 1:1 W/Y mixture, and trans-WY dipeptide. The relative intensity of intermode correlation can be directly viewed by cross peaks in the 2DSRR spectra. Correlations between specific vibrational modes can be examined by proper pulse configurations. The W/Y mixture and WY dipeptide can be better distinguished by time-domain multidimensional Raman spectroscopy than by spontaneous Raman techniques. Multidimensional UV stimulated resonance Raman technique could be a useful tool for protein secondary structure determination.

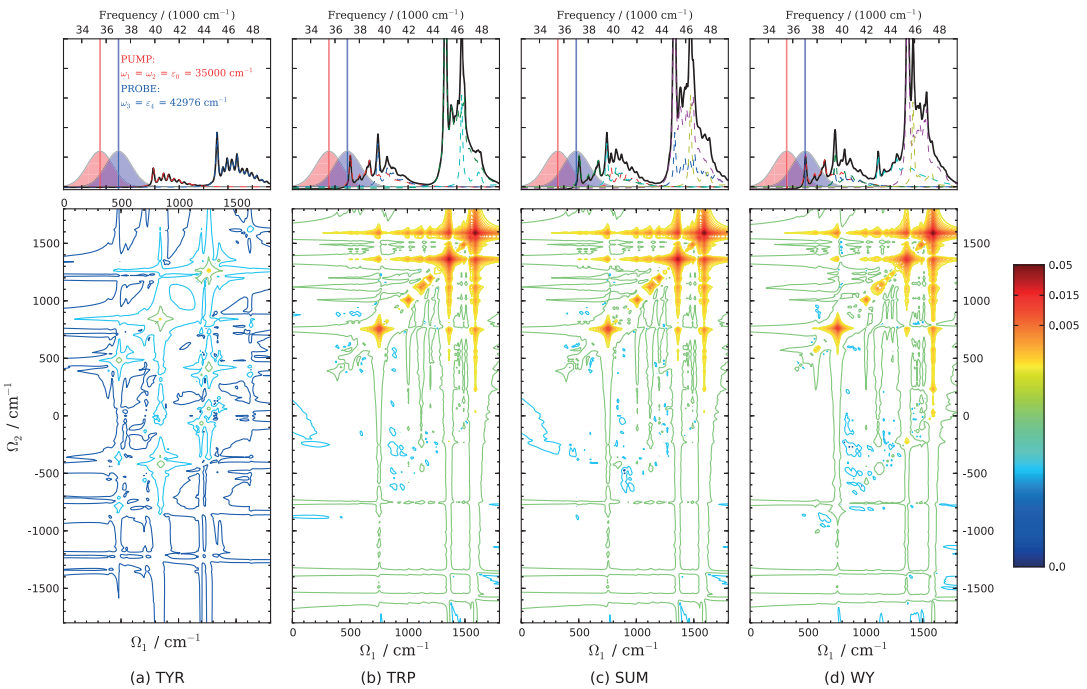

Figure 13. Two-dimensional simulated resonance Raman spectra of (a) tyrosine, (b) tryptophan, (c) 1:1 mixture (sum of (a) and (b)), and (d) WY dipeptide for $\omega_1 = \omega_2 = \varepsilon_0$ and $\omega_3 = \varepsilon_1$. Pulse envelopes and the absorption spectra are shown on top. This figure is available in colour online at wileyonlinelibrary.com/journal/jrs.

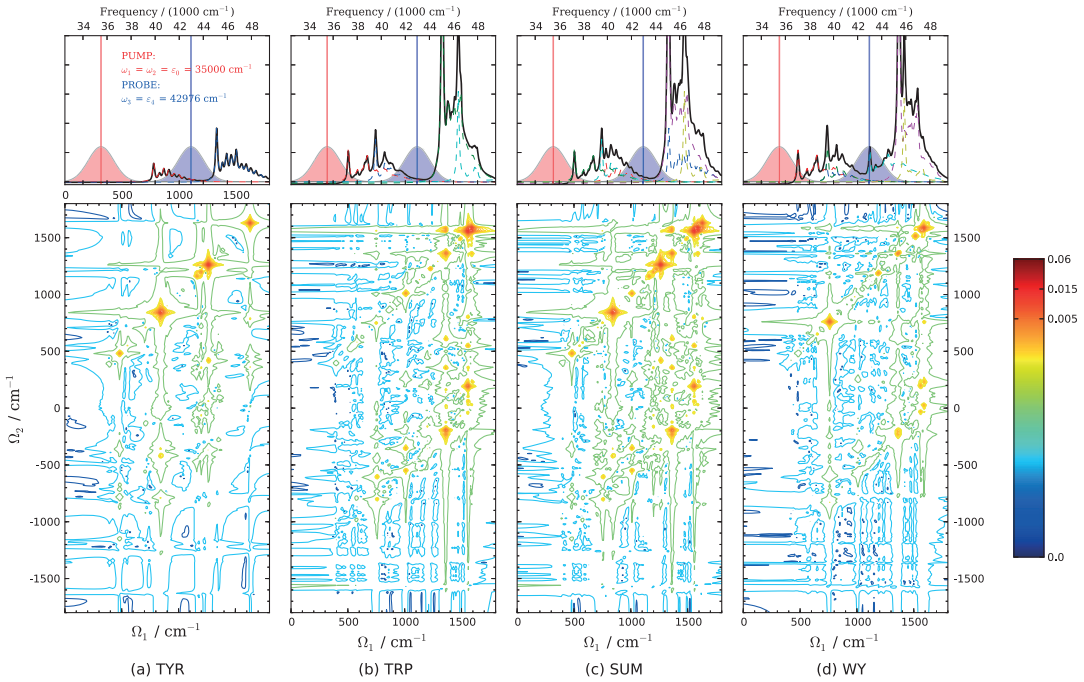

Figure 14. Same as Figure 13, except for $\omega_1 = \omega_2 = \varepsilon_0$ and $\omega_3 = \varepsilon_4$. This figure is available in colour online at wileyonlinelibrary.com/journal/jrs.

Acknowledgements

We gratefully acknowledge the support of the National Institutes of Health (grant GM059230), the National Science Foundation (grant CHE-1058791), and the Chemical Sciences, Geosciences and Biosciences Division, Office of Basic energy Sciences, Office of Science, US Department of Energy (grant DE-FG02-04ER15571). We acknowledge the computational resource support from the GreenPlanet cluster at UCI (NSF Grant CHE-0840513).

Appendix A

The cumulant expansion for transition polarizabilities

The matrix element for the effective polarizability $\alpha_{ca}^{(m)} \equiv \langle c|\hat{\alpha}^{(m)}|a\rangle$ defined in Eqn (10) is the transition amplitude to go from state $|a\rangle$ to state $|c\rangle$, obtained by summing over all intermediate vibronic states $|b\rangle$ lying within the bandwidth of the mth pulse. The number of excited states $|b\rangle$ scales exponentially with the number of vibrational modes, and a full summation becomes impractical. By treating the Raman inactive modes via the cumulant expansion,[2] we greatly reduce computational cost.

We define the ground state

$$\left|\psi_g^0\right\rangle \equiv \prod_j \left|(0)_g^j\right\rangle \tag{A1}$$

i.e. $\left|(n)_g^j\right\rangle$ is a single-mode wave function with n quanta of vibrational excitation, in the ground electronic state. The state with a single quantum of excitation in the jth mode is

$$\left|(1)_g^j\right\rangle_0 = \hat{b}_j^\dagger \left|\psi_g^0\right\rangle \tag{A2}$$

where the 0 subscript is used to distinguish the many-body wavefunction $\left|(1)_g^j\right\rangle_0$ from the single-mode wavefunction $\left|(1)_g^j\right\rangle$ and $\hat{b}_j^\dagger$ is the creation operator that corresponds to the single quantum vibrational excitation in the jth mode. Similarly, we define overtones (doubly excited state)

$$\left|(2)_g^j\right\rangle_0 = \hat{b}_j^\dagger \hat{b}_j^\dagger \left|\psi_g^0\right\rangle \tag{A3}$$

and the combination states

$$\left|(1)_g^j (1)_g^k\right\rangle_0 = \hat{b}_j^\dagger \hat{b}_k^\dagger \left|\psi_g^0\right\rangle \tag{A4}$$

In the calculations presented here, the contributions of overtone and combination bands are weak and were neglected; however, we provide the formulas here for the sake of completeness.

The Raman process involves up-and-down transitions induced by fields E_j and E_j^*. The transition polarizability amplitude is given by

$$\begin{aligned} {}_0\left\langle (1)_g^j \middle| \alpha^{(m)} \middle| \psi_g^0 \right\rangle &= -i \int_{-\infty}^{\infty} dt_2 \int_{-\infty}^{t_2} dt_1 E_m^*(t_2) E_m(t_1)_0 \\ &\times \left\langle (1)_g^j \middle| V(t_2) V(t_1) \middle| \psi_g^0 \right\rangle \end{aligned} \tag{A5}$$

Here, $V(t)$ is the dipole operator in the interaction picture

$$V(t) \equiv e^{iHt} \sum_e \left(\mu_{ge}|g\rangle\langle e| + \mu_{eg}|e\rangle\langle g|\right) e^{-iHt} \tag{A6}$$

The dipole correlation function may be expanded as

$$\begin{aligned} {}_0\left\langle (1)_g^j \middle| \alpha^{(m)} \middle| \psi_g^0 \right\rangle &= \sum_e -i \int_{-\infty}^{\infty} \mathrm{d}t_2 \int_{-\infty}^{t_2} \mathrm{d}t_1 E_m^*(t_2) E_m(t_1) \\ &\times \left\langle (1)_g^j \middle| e^{iH_g^j t_2} e^{-iH_e^j (t_2 - t_1)} e^{-iH_g^j t_1} \middle| (0)_g^j \right\rangle \\ &\times \langle V(t_2 - t_1) V(0) \rangle_{j'} \end{aligned} \tag{A7}$$

where the prime in the subscript j' denotes that the contribution of the jth mode is excluded in that correlation function. The single-mode correlation function can be handled by inserting resolution of the identity

$$\left\langle (1)_g^j \middle| e^{i\mathbf{H}_g^j t_2} e^{-i\mathbf{H}_e^j (t_2-t_1)} e^{-i\mathbf{H}_g^j t_1} \middle| (0)_g^j \right\rangle = \sum_e \sum_a \left\langle (1)_g^j \middle| (a)_e^j \right\rangle \left\langle (a)_e^j \middle| (0)_g^j \right\rangle \exp\left[i\omega_j t_2 - ia\omega_j (t_2 - t_1) \right] \tag{A8}$$

The Frank–Condon factors were calculated in the standard way.[53]

The second correlation function represents the spectator Raman inactive vibrational modes and is evaluated by the cumulant expansion[2]

$$\langle V(t_2 - t_1) V(0) \rangle_{j'} \equiv \sum_e \prod_{k \neq j} \left\langle (0)_g^k \middle| e^{i\mathbf{H}_g^k (t_2 - t_1)} \mu e^{-i\mathbf{H}_e^k (t_2 - t_1)} \mu \middle| (0)_g^k \right\rangle = \sum_e \left| \mu_{eg} \right|^2 \exp\left[-i\omega_{eg}^{j'} (t_2 - t_1) - g_e^{j'} (t_2 - t_1) \right] \tag{A9}$$

where the electronic excitation frequency and line shape function are defined as

$$\omega_{eg}^{j'} = \varepsilon_e + \sum_{k \neq j} \frac{(\Delta_e^j)^2}{2} \omega_k \tag{A10}$$

and

$$g_e^{j'}(t) \equiv \sum_{k \neq j} \frac{(\Delta_e^j)^2}{2} \left\{ coth\left(\frac{\beta \omega_k}{2} \right) [1 - \cos(\omega_k t)] + i[\sin(\omega_k t) - \omega_k t] \right\} \tag{A11}$$

Here, $\beta = (kT)^{-1}$ is the inverse temperature. The effective transition polarizability now reads

$$ {}_0\left\langle (1)_g^j \middle| \alpha^{(m)} \middle| \psi_g^0 \right\rangle = \sum_e -i|\mu_{eg}|^2 \sum_a \left\langle (1)_g^j \middle| (a)_e^j \right\rangle \times \left\langle (a)_e^j \middle| (0)_g^j \right\rangle \int_{-\infty}^{\infty} dt_2 \int_{-\infty}^{t_2} dt_1 E_m^*(t_2) E_m(t_1) \times \exp[i\omega_j t_2 - ia\omega_j (t_2 - t_1) - i\omega_{eg}^{j'} (t_2 - t_1) - g_e^{j'} (t_2 - t_1)] \tag{A12}$$

We take $E(t)$ to be Gaussian:

$$E_m(t) = \frac{1}{\pi^{1/4} \sigma_m^{1/2}} e^{-t^2/2\sigma_m^2 - i\omega_m t} \tag{A13}$$

Substituting Eqn (A13) into Eqn (A12) gives

$$ {}_0\left\langle (1)_g^j \middle| \alpha^{(m)} \middle| \psi_g^0 \right\rangle = \sum_{e,a} -i|\mu_{eg}|^2 \left\langle (1)_g^j \middle| (a)_e^j \right\rangle \left\langle (a)_e^j \middle| (0)_g^j \right\rangle e^{-\sigma_m^2 \omega_j^2/4} \times \int_{-\infty}^{\infty} dt \; e^{i\omega_m t} \exp\left[-\frac{t^2}{4\sigma_m^2} - i\omega_{eg}^{j'} t - i\left(a - \frac{1}{2} \right) \omega_j t - g_e^{j'}(t) - \gamma_{eg} t \right] \theta(t) \tag{A14}$$

Eqn (A14) was evaluated by a fast Fourier transform. Matrix elements such as ${}_0\left\langle (2)_g^j \middle| \alpha \middle| \psi_g^0 \right\rangle$ and ${}_0\left\langle (1)_g^j (1)_g^k \middle| \alpha \middle| \psi_g^0 \right\rangle$ may be obtained in the same manner and are provided here for completeness:

$$ {}_0\left\langle (2)_g^j \middle| \alpha^{(m)} \middle| \psi_g^0 \right\rangle = \sum_{e,a} -i|\mu_{eg}|^2 \left\langle (2)_g^j \middle| (a)_e^j \right\rangle \left\langle (a)_e^j \middle| (0)_g^j \right\rangle e^{-\sigma_m^2 \omega_j^2} \times \int_{-\infty}^{\infty} dt e^{i\omega_m t} \exp\left[-\frac{t^2}{4\sigma_m^2} - i\omega_{eg}^{j'} t - i(a-1) \times \omega_j t - g_e^{j'}(t) - \gamma_{eg} t \right] \theta(t) \tag{A15}$$

$$ {}_0\left\langle (1)_g^j (1)_g^k \middle| \alpha^{(m)} \middle| \psi_g^0 \right\rangle = \sum_{e,a,b} -i|\mu_{eg}|^2 \left\langle (1)_g^j \middle| (a)_e^j \right\rangle \left\langle (a)_e^j \middle| (0)_g^j \right\rangle \times \left\langle (1)_g^k \middle| (b)_e^k \right\rangle \left\langle (b)_e^k \middle| (0)_g^k \right\rangle e^{-\sigma_m^2 (\omega_j + \omega_k)^2/4} \times \int_{-\infty}^{\infty} dt e^{i\omega_m t} \exp\left[-\frac{t^2}{4\sigma_m^2} - i\omega_{eg}^{j'k'} t - i\left(a - \frac{1}{2} \right) \omega_j t - i\left(b - \frac{1}{2} \right) \omega_k t - g_e^{j'k'}(t) - \gamma_{eg} t \right] \theta(t) \tag{A16}$$

A 2D stimulated Raman signal requires matrix elements between vibrationally excited states, and these are given as follows:

$$ {}_0\left\langle (1)_g^j \middle| \alpha^{(m)} \middle| (1)_g^k \right\rangle_0 = \sum_{e,a,b} -i|\mu_{eg}|^2 \left\langle (1)_g^j \middle| (a)_e^j \right\rangle \left\langle (a)_e^j \middle| (0)_g^j \right\rangle \times \left\langle (0)_g^k \middle| (b)_e^k \right\rangle \left\langle (b)_e^k \middle| (1)_g^k \right\rangle e^{-\sigma_m^2 (\omega_j - \omega_k)^2/4} \times \int_{-\infty}^{\infty} dt e^{i\omega_m t} \exp\left[-\frac{t^2}{4\sigma_m^2} - i\omega_{eg}^{j'k'} t - i\left(a - \frac{1}{2} \right) \omega_j t + i\left(b - \frac{1}{2} \right) \omega_k t - g_e^{j'k'}(t) - \gamma_{eg} t \right] \theta(t) \tag{A17}$$

$$ {}_0\left\langle (2)_g^j \middle| \alpha^{(m)} \middle| (1)_g^k \right\rangle_0 = \sum_{e,a,b} -i|\mu_{eg}|^2 \left\langle (2)_g^j \middle| (a)_e^j \right\rangle \left\langle (a)_e^j \middle| (0)_g^j \right\rangle \times \left\langle (0)_g^k \middle| (b)_e^k \right\rangle \left\langle (b)_e^k \middle| (1)_g^k \right\rangle e^{-\sigma_m^2 (2\omega_j - \omega_k)^2/4} \times \int_{-\infty}^{\infty} dt e^{i\omega_m t} \exp\left[-\frac{t^2}{4\sigma_m^2} - i\omega_{eg}^{j'k'} t - i\left(a - \frac{1}{2} \right) \omega_j t + i(b-1) \omega_k t - g_e^{j'k'}(t) - \gamma_{eg} t \right] \theta(t) \tag{A18}$$

$$ {}_0\left\langle (2)_g^j \middle| \alpha^{(m)} \middle| (2)_g^k \right\rangle_0 = \sum_{e,a,b} -i|\mu_{eg}|^2 \left\langle (2)_g^j \middle| (a)_e^j \right\rangle \left\langle (a)_e^j \middle| (0)_g^j \right\rangle \times \left\langle (0)_g^k \middle| (b)_e^k \right\rangle \left\langle (b)_e^k \middle| (2)_g^k \right\rangle e^{-\sigma_m^2 (\omega_j - \omega_k)^2} \times \int_{-\infty}^{\infty} dt e^{i\omega_m t} \exp\left[-\frac{t^2}{4\sigma_m^2} - i\omega_{eg}^{j'k'} t - i(a-1) \omega_j t + i(b-1) \omega_k t - g_e^{j'k'}(t) - \gamma_{eg} t \right] \theta(t) \tag{A19}$$

$$
\begin{aligned}
{}_0\left\langle (1)_g^j \middle| \alpha^{(m)} \middle| (1)_g^k (1)_g^l \right\rangle_0 = \sum_{e,a,b,c} -i|\mu_{eg}|^2 \left\langle (1)_g^j \middle| (a)_e^j \right\rangle \left\langle (a)_e^j \middle| (0)_g^j \right\rangle \\
\times \left\langle (0)_g^k \middle| (b)_e^k \right\rangle \left\langle (b)_e^k \middle| (1)_g^k \right\rangle \times \left\langle (0)_g^l \middle| (c)_e^l \right\rangle \\
\times \left\langle (c)_e^l \middle| (1)_g^l \right\rangle e^{-\sigma_m^2 \left(\omega_j - \omega_k - \omega_l\right)^2/4} \\
\times \int_{-\infty}^{\infty} dt e^{i\omega_m t} \exp[-\frac{t^2}{4\sigma_m^2} - i\omega_{eg}^{j'k'l'} t \\
-i\left(a - \frac{1}{2}\right)\omega_j t] \times \exp[i\left(b - \frac{1}{2}\right)\omega_k t \\
+i\left(c - \frac{1}{2}\right)\omega_l t - g_e^{j'k'l'}(t) - \gamma_{eg} t]\theta(t)
\end{aligned}
\tag{A20}
$$

$$
\begin{aligned}
{}_0\left\langle (2)_g^j \middle| \alpha^{(m)} \middle| (1)_g^k (1)_g^l \right\rangle_0 = \sum_{e,a,b,c} -i|\mu_{eg}|^2 \left\langle (2)_g^j \middle| (a)_e^j \right\rangle \left\langle (a)_e^j \middle| (0)_g^j \right\rangle \\
\times \left\langle (0)_g^k \middle| (b)_e^k \right\rangle \left\langle (b)_e^k \middle| (1)_g^k \right\rangle \times \left\langle (0)_g^l \middle| (c)_e^l \right\rangle \\
\times \left\langle (c)_e^l \middle| (1)_g^l \right\rangle e^{-\sigma_m^2 \left(2\omega_j - \omega_k - \omega_l\right)^2/4} \\
\times \int_{-\infty}^{\infty} dt e^{i\omega_m t} \exp[-\frac{t^2}{4\sigma_m^2} - i\omega_{eg}^{j'k'l'} t \\
-i(a-1)\omega_j t] \quad \times \exp[i\left(b - \frac{1}{2}\right)\omega_k t \\
+i\left(c - \frac{1}{2}\right)\omega_l t - g_e^{j'k'l'}(t) - \gamma_{eg} t]\theta(t)
\end{aligned}
\tag{A21}
$$

$$
\begin{aligned}
{}_0\left\langle (1)_g^j (1)_g^k \middle| \alpha^{(m)} \middle| (1)_g^l (1)_g^n \right\rangle_0 = \sum_{e,a,b,c,d} -i|\mu_{eg}|^2 \left\langle (1)_g^j \middle| (a)_e^j \right\rangle \\
\times \left\langle (a)_e^j \middle| (0)_g^j \right\rangle \left\langle (1)_g^k \middle| (b)_e^k \right\rangle \left\langle (b)_e^k \middle| (0)_g^k \right\rangle \\
\times \left\langle (0)_g^l \middle| (c)_e^l \right\rangle \left\langle (c)_e^l \middle| (1)_g^l \right\rangle \left\langle (0)_g^n \middle| (d)_e^n \right\rangle \\
\times \left\langle (d)_e^n \middle| (1)_g^n \right\rangle e^{-\sigma_m^2 \left(\omega_j + \omega_k - \omega_l - \omega_n\right)^2/4} \\
\times \int_{-\infty}^{\infty} dt e^{i\omega_m t} \exp[-\frac{t^2}{4\sigma_m^2} - i\omega_{eg}^{j'k'l'} t \\
-i\left(a - \frac{1}{2}\right)\omega_j t - i\left(b - \frac{1}{2}\right)\omega_k t] \\
\times \exp[i\left(c - \frac{1}{2}\right)\omega_l t + i\left(d - \frac{1}{2}\right)\omega_n t \\
-g_e^{j'k'l'}(t) - \gamma_{eg} t]\theta(t)
\end{aligned}
\tag{A22}
$$

We set $E_m(t) = exp(-i\omega_1 t)$ and $E_m^*(t) = exp(i\omega_2 t)$ in Eqn (A12). Performing one integration gives $\delta(\omega_1 - \omega_2 - \omega_j)$ and adding a phenomenological electronic lifetime, we arrive at

$$
\begin{aligned}
{}_0\left\langle (1)_g^j \middle| \alpha \middle| \psi_g^0 \right\rangle = \sum_{e,a} -i|\mu_{eg}|^2 \left\langle (1)_g^j \middle| (a)_e^j \right\rangle \left\langle (a)_e^j \middle| (0)_g^j \right\rangle \\
\times \int_{-\infty}^{\infty} dt e^{i\omega_1 t} \exp\left[-i\left(\omega_{eg}^j + a\omega_j\right)t - g_e^j(t) - \gamma_{eg} t\right]\theta(t)
\end{aligned}
\tag{A23}
$$

Eqn (A23) can be calculated by a fast Fourier transform. Other matrix elements of α can be readily obtained.

Appendix B

Relative strength of ground state and excited state contributions as a function of detuning

It can easily be shown that the excited state contribution to a pump–probe signal decays much more quickly with pulse detuning than the ground state contribution using a simple three-state model. This model includes the ground state, $|a\rangle$, an electronically excited state, $|b\rangle$, and a vibrationally excited state, $|c\rangle$, with energies such that $\omega_{ba} \gg \omega_{ca} > 0$. Interaction with the pump pulse will place amplitude in the electronically and vibrationally excited states, $|\psi_e\rangle$ and $|\psi_g\rangle$, respectively. The excited state contribution to a pump–probe signal is proportional to the population in state $|b\rangle$ after interaction with the pump pulse (Eqn (A13)) and is given by

$$
\langle \psi_e | \psi_e \rangle = \frac{\sigma}{2\sqrt{\pi}} |\mu_{ab}|^2 e^{-d^2} \tag{B1}
$$

where $d \equiv \sigma(\Omega - \omega_{ba})$ is the effective detuning. The SRS contribution to the pump–probe signal is proportional to the amplitude in state $|c\rangle$ after interaction with the pump pulse, given by

$$
\sqrt{\left\langle \psi_g \middle| \psi_g \right\rangle} = \frac{\sigma}{\sqrt{\pi}} \mu_{cb}\mu_{ba} e^{-\sigma^2\omega_{ca}^2} \left| e^{-(d+\sigma\omega_{ca}/2)^2} + \frac{2}{\sqrt{\pi}} F(d + \sigma\omega_{ca}/2) \right| \tag{B2}
$$

Here, $F(x) \equiv e^{-x^2} \int_0^x dy e^{y^2}$ is Dawson's integral,[54] which has the following asymptotic series (truncated at some finite order, valid for large x):

$$
F(x) \sim \frac{1}{2x}\left(1 + \frac{1}{2x^2} + \sum_{n=2} \frac{(2n-1)!!}{2^n x^{2n}}\right) \tag{B3}
$$

As the detuning becomes large, the Gaussian term inside the brackets of Eqn (B2) becomes small and can be neglected. Keeping the leading term of Eqn (B3), the $|c\rangle$ amplitude can be written in the limit of large detuning as

$$
\sqrt{\left\langle \psi_g \middle| \psi_g \right\rangle} \simeq \frac{2\sigma}{\pi} \mu_{cb}\mu_{ba} e^{-\sigma^2\omega_{ca}^2} \left| \frac{1}{2(d + \sigma\omega_{ca}/2)} \right|. \tag{B4}
$$

The necessary resonance offset for the stimulated Raman signals calculated and presented in the 1DSRR Spectra and 2DSRR Spectra sections was determined by finding that center frequency such that B5

$$
\frac{\langle \psi_e | \psi_e \rangle}{\sqrt{\left\langle \psi_g \middle| \psi_g \right\rangle}} \leq 0.1 \tag{B5}
$$

The numerator and denominator in Eqn (B5) were both calculated using the displaced harmonic oscillator Hamiltonian and cumulant expansion method presented in Appendix A.

Supporting information

Supporting information may be found in the online version of this article.

References

[1] L. D. Ziegler, P. M. Champion (Eds). *XXII International Conference on Raman Spectroscopy*, AIP Conference Proceedings, Vol. *1267*, AIP Press: Boston, **2010**.
[2] S. Mukamel, *Principles of Nonlinear Optical Spectroscopy*, 1st ed. Oxford University Press, New York Oxford, **1995**.
[3] C. Huang, G. Balakrishnan, T. G. Spiro, *J. Raman Spectrosc.* **2006**, *37*, 277.
[4] A. Soldatova, M. Ibrahim, J. Olson, R. Czernuszewicz, T. Spiro, *J. Am. Chem. Soc.* **2010**, *132*, 4614.
[5] A. Ozdemir, I. K. Lednev, S. A. Asher, *Spectrochim. Acta Part A* **2005**, *61*, 19.
[6] A. Mikhonin, Z. Ahmed, A. Ianoul, S. Asher, *J. Phys. Chem. B* **2004**, *108*, 19020.
[7] L. A. Popova, R. Kodali, R. Wetzel, I. K. Lednev, *J. Am. Chem. Soc.* **2010**, *132*, 6324.
[8] A. V. Mikhonin, S. V. Bykov, N. S. Myshakina, S. A. Asher, *J. Phys. Chem. B* **2006**, *110*, 1928.
[9] A. V. Mikhonin, S. A. Asher, *J. Phys. Chem. B* **2005**, *109*, 3047.
[10] S. A. Asher, A. Ianoul, G. Mix, M. N. Boyden, A. Karnoup, M. Diem, R. Schweitzer-Stenner, *J. Am. Chem. Soc.* **2001**, *123*, 11775.
[11] H. Ren, J. Jiang, S. Mukamel, *J. Phys. Chem. B* **2011**, *115*, 13955.
[12] D. Kurouski, W. Lauro, I. K. Lednev, *Chem. Commun.* **2010**, *46*, 4205.
[13] S. Oladepo, K. Xiong, Z. Hong, S. Asher, *J. Phys. Chem. Lett.* **2011**, *2*, 334.
[14] A. Sato, Y. Gao, T. Kitagawa, Y. Mizutani, *Proc. Natl. Acad. Sci. U. S. A.* **2007**, *104*, 9627.
[15] B. Quan, A. Ianoul, *J. Raman Spectrosc.* **2009**, *40*, 260.
[16] H. Shafaat, B. Leigh, M. Tauber, J. Kim, *J. Phys. Chem. B* **2008**, *113*, 382.
[17] M. Kubo, F. Gruia, A. Benabbas, A. Barabanschikov, W. Montfort, E. Maes, P. Champion, *J. Am. Chem. Soc.* **2008**, *130*, 9800.
[18] C. Pohling, T. Buckup, M. Motzkus, *J. Biomed. Opt.* **2011**, *16*, 021105.
[19] P. Kukura, D. W. McCamant, R. A. Mathies, *Annu. Rev. Phys. Chem.* **2007**, *58*, 461.
[20] H. Kuramochi, S. Takeuchi, T. Tahara, *J. Phys. Chem. Lett.* **2012**, *3*, 2025.
[21] S. Shim, J. Dasgupta, R. Mathies, *J. Am. Chem. Soc.* **2009**, *131*, 7592.
[22] B. Mallick, A. Lakhsmanna, S. Umapathy, *J. Raman Spectrosc.* **2011**, *42*, 1883.
[23] E. Ploetz, B. Marx, P. Gilch, *J. Raman Spectrosc.* **2010**, *41*, 609.
[24] Y. Tanimura, S. Mukamel, *J. Chem. Phys.* **1993**, *99*, 9496.
[25] U. Selig, C.-F. Schleussner, M. Foerster, F. Langhojer, P. Nuernberger, T. Brixner, *Opt. Lett.* **2010**, *35*, 4178.
[26] C. hung Tseng, S. Matsika, T. C. Weinacht, *Opt. Express* **2009**, *17*, 18788.
[27] S. Ruetzel, M. Kullmann, J. Buback, P. Nuernberger, T. Brixner, In *XVIIIth International Conference on Ultrafast Phenomena*, (Ed.: M. Chergui), Lausanne, **2012**.
[28] G. Auboeck, C. Consani, F. van Mourik, M. Chergui, *Opt. Lett.* **2012**, *37*, 2337.
[29] B. A. West, A. M. Moran, *J. Phys. Chem. Lett.* **2012**, *3*, 2575.
[30] C. Homann, P. Lang, E. Riedle, *J. Opt. Soc. Am. B* **2012**, *29*, 2765.
[31] P. Harmon, J. Teraoka, S. Asher, *J. Am. Chem. Soc.* **1990**, *112*, 8789.
[32] R. Rava, T. Spiro, *J. Phys. Chem.* **1985**, *89*, 1856.
[33] J. Jiang, S. Mukamel, *Phys. Chem. Chem. Phys.* **2011**, *13*, 2394.
[34] E. V. Tsiper, V. Chernyak, S. Tretiak, S. Mukamel, *Chem. Phys. Lett.* **1999**, *302*, 77.
[35] A. B. Myers, R. A. Mathies, D. J. Tannor, E. J. Heller, *J. Chem. Phys.* **1982**, *77*, 3857.
[36] J. D. Biggs, J. A. Voll, S. Mukamel, *Phil. Trans. R. Soc. A* **2012**, *370*, 3709.
[37] J. D. Biggs, Y. Zhang, D. Healion, S. Mukamel, *J. Chem. Phys.* **2012**, *136*, 174117.
[38] G. H. Zschornack, *Handbook of X-ray data*, 1st ed. Springer-Verlag GmbH: Leipzig, **2007**.
[39] C. Pokalsky, P. Wick, E. Harms, F. Lytle, R. V. Etten, *J. Bio. Chem.* **1995**, *270*, 3809.
[40] Y. J. Yan, S. Mukamel, *J. Chem. Phys.* **1991**, *94*, 997.
[41] M. J. Frisch, G. W. Trucks, H. B. Schlegel, G. E. Scuseria, M. A. Robb, J. R. Cheeseman, G. Scalmani, V. Barone, B. Mennucci, G. A. Petersson, Nakatsuji, M. Caricato, X. Li, H. P. Hratchian, A. F. Izmaylov, J. Bloino, G. Zheng, J. L. Sonnenberg, M. Hada, M. Ehara, K. Toyota, R. Fukuda, J. Hasegawa, M. Ishida, T. Nakajima, Y. Honda, O. Kitao, H. Nakai, T. Vreven, J. A. Montgomery, Jr., J. E. Peralta, F. Ogliaro, M. Bearpark, J. J. Heyd, E. Brothers, K. N. Kudin, V. N. Staroverov, R. Kobayashi, J. Normand, K. Raghavachari, A. Rendell, J. C. Burant, S. S. Iyengar, J. Tomasi, M. Cossi, N. Rega, J. M. Millam, M. Klene, J. E. Knox, J. B. Cross, V. Bakken, C. Adamo, J. Jaramillo, R. Gomperts, R. E. Stratmann, O. Yazyev, A. J. Austin, R. Cammi, C. Pomelli, J. W. Ochterski, R. L. Martin, K. Morokuma, V. G. Zakrzewski, G. A. Voth, P. Salvador, J. J. Dannenberg, S. Dapprich, A. D. Daniels, Ö. Farkas, J. B. Foresman, J. V. Ortiz, J. Cioslowski, D. J. Fox, *Gaussian 09 Revision C.01*, Gaussian Inc. Wallingford CT, **2009**.
[42] J. P. Perdew, K. Burke, M. Ernzerhof, *Phys. Rev. Lett.* **1996**, *77*, 3865.
[43] R. D. Amos, *Chem. Phys. Lett.* **1982**, *87*, 23.
[44] V. Barone, M. Cossi, *J. Phys. Chem. A* **1998**, *102*, 1995.
[45] M. Cossi, N. Rega, G. Scalmani, V. Barone, *J. Comput. Chem.* **2003**, *24*, 669.
[46] A. P. Scott, L. Radom, *J. Phys. Chem.* **1996**, *100*, 16502.
[47] J. P. Merrick, D. Moran, L. Radom, *J. Phys. Chem. A* **2007**, *111*, 11683.
[48] J. R. Platt, *J. Chem. Phys.* **1949**, *17*, 484.
[49] R. Martin, *J. Chem. Phys.* **2003**, *118*, 4775.
[50] C. Adamo, V. Barone, *Chem. Phys. Lett.* **1999**, *314*, 152.
[51] S. Mukamel, A. Piryatinski, V. Chernyak, *Acc. Chem. Res.* **1999**, *32*, 145.
[52] C. Manneback, *Physica* **1951**, *17*, 1001.
[53] M. Abramowitz, I. Stegun, *Handbook of Mathematical Functions*, Dover Publications Inc., New York, **1972**.
[54] E. Wilson, *Phys. Rev.* **1934**, *45*, 706.
[55] R. P. Rava, T. G. Spiro, *J. Am. Chem. Soc.* **1984**, *106*, 4062.